Inflation of Okmok volcano during 2008 to 2020 from PS analyses and source inversion with finite element models

- 4 Jiahui Wang 1, Zhong Lu 1, and Patricia M. Gregg 2
- ¹Southern Methodist University, Dallas, TX, United States
- ²University of Illinois at Urbana-Champaign, Champaign, IL, United States
- 7 Corresponding author: Zhong Lu (zhonglu@mail.smu.edu)
- **8** Key Points:

2

3

9

10

11

12

13

- The deformation history of Okmok from 2008 to 2020 is mapped with satellite interferometric synthetic aperture radar
- A time-dependent finite element model for the magma source is developed using ensemble Kalman filter
- The cumulative volume change during 2008-2020 is \sim 160% and \sim 60% of the total volumes of the 1997 and the 2008 eruptions

Abstract

Okmok volcano, located on northeastern Umnak Island along the eastern end of the Aleutian island arc, is one of the most active volcanoes in Alaska, producing multiple eruptions in the past century. The most recent eruption, which occurred during July-August of 2008, was the most explosive since the early nineteenth century. In the years following the 2008 eruption, Global Navigation Satellite System (GNSS) and Interferometric Synthetic Aperture Radar (InSAR) observations indicate that Okmok has inflated at a variable rate of 40-195 mm/yr. In this study, we investigate the post-eruptive deformation of Okmok (2008-2020) using InSAR and GNSS. L-band ALOS-2, C-band Sentinel-1/Envisat and X-band TerraSAR-X data are analyzed with Persistent Scatterer (PS) InSAR method. The deformation time series calculated from InSAR and GNSS are assimilated into finite element models (FEMs) using the Ensemble Kalman Filter (EnKF) to track the evolution of the magma system through time. The results indicate that the InSAR-derived deformation history can be well explained by a spatially stable magmatic source located in the central caldera, at about 3 km beneath the sea level, which is also believed to be the same source that produced the 1997 and 2008 eruptions. Magma accumulation in the reservoir is about $0.08 \, km^3$ from 2008 to 2020, which is about 160% and about 60% of the total reservoir volume changes during the 1997 and the 2008 eruptions, respectively.

Plain Language Summary

Precise mapping of volcano deformation allows for identification and modeling of the source location, shape, and pressure change within a magma reservoir of the volcanic system. Hence, monitoring ground surface deformation is a critical part in volcano study and eruption forecasting. In this study, we map the deformation history of Okmok volcano since its 2008 eruption using InSAR. The produced displacement time series are then used to track the magmatic pressure accumulation in the magmatic reservoir with numerical models. Our InSAR measurements show that Okmok has been undergoing persistent inflation with time-varying rates since the last eruption in 2008. The measured deformation suggests the magmatic source as that accounting for the pre-2008 eruptions. The cumulative volume change during 2008-2020 is ~160% and ~60% of the total volumes of the 1997 and the 2008 eruptions, respectively.

1 Introduction

Okmok, located in the northeast of the Umnak Island, Alaska, is one of the most activate volcanoes in the Aleutian Island Arc. Two major catastrophic pyroclastic eruptions with max Volcanic Explosivity Index (VEI) exceeded 4, i.e., Okmok Caldera Forming Eruption (CFE) I and Okmok CFE II dated about 12000 years and 2050 ¹⁴C years ago, respectively, shaped the major topographic morphology of Okmok (Larsen et al., 2007; Byers, 1959). In addition to the current caldera rim, evidence from six arctic ice cores shows the Okmok CFE II may also be responsible for one of the coldest decades of recent millennia in the Northern Hemisphere (McConnell et al., 2020). Since 1900, multiple effusive eruptions have been documented at Okmok producing a new prominent cone, Cone A. From 1943 to 1997, all of Okmok's eruptions have originated from Cone A (Figure 1; Lu and Dzurisin, 2014). The most recent eruption in 2008, spanned from July 12 to mid-August, was the most explosive eruption since at least the

late nineteenth century, and produced a minimum of 0.17 km^3 of dense rock-equivalent ejecta (Larsen et al., 2015). As opposed to previous eruptions, the 2008 eruption emanated from the northwest flank of an existing cinder cone (Cone D), about 5 km northeast of Cone A. Due to the strong magma interaction with ground and surface water, the 2008 eruption was highly phreatomagmatic (Larsen et al., 2013; 2015). The ejected ash and tephra deposit during the 2008 eruption covered the entire caldera and part of the northeast flank of the caldera and formed a new tuff cone near Cone D (named "Ahmanilix"; Larsen et al., 2015).

59

60

61

62

63

64

65 66

67

68

69 70

71 72

73

74

75

Figure 1. Location and topography of Okmok volcano. The elevation data is from ArcticDEM. Global Positioning System (GPS) stations used in this study are labelled with blue stars. Cone E, Cone A, Cone D and Ahmanilix are labeled with red triangle. Inset at the lower-right corner indicates the location of the Okmok volcano in the Aleutian arc.

Due to the remote location and small population of Umnak Island, most of Okmok's historical eruptions are poorly documented. Thanks to the advance in spaceborne geodetic techniques, the 1997 and 2008 eruptions were well observed and documented. The magma source and eruption mechanisms have been previously studied using ground deformation

measurements from InSAR and GPS data. Before the 1997 eruption, inflation with a decreasing 76 rate was observed from 1992 to 1995 and stalled sometime during 1995 to 1996, during which 77 stage slight local subsidence occurred instead (Lu et al., 2000; Mann et al., 2002). The pre-78 79 eruption inflation was interpreted as the result of accumulation of magma, the local deflation may have been related to withdrawal or movement of the magma or hydrothermal 80 depressurization (Mann et al., 2002). Since the first post-eruption observation in 1997, persistent 81 inflation at a varying rate was confirmed by both InSAR and GPS. Episodic pulses of more rapid 82 inflation signals were observed during 1997-1998 and 2001-2003. The deformation rate 83 decreased and the caldera subsided 3-5 cm during 2004-2005, and then elevated a similar amount 84 during 2005-2006. Preceding the 2008 eruption, uplift of ~150 mm/yr was recorded during 85 2007-2008 (Fournier et al., 2009; Lu et al., 2010). Based on the deformation signal from 1992 to 86 2008 derived from multiple InSAR datasets, Lu et al. (2010, 2005) inferred a tension sphere 87 (Mogi) source embedded ~3 km below sea level (BSL). Fournier et al. (2009) derived a stable 88 Mogi source at ~2.5 km BSL with both campaign and continuous GPS data spanning from 2000 89 to 2007. Biggs et al. (2010) found a Mogi source at a depth of ~3.4 km using a combined dataset 90 consisted of GPS data spanning from 2000 to 2007 and InSAR data from 1992 to 2007. Lu et al. 91 (2010) found a Mogi source with a depth evolving from ~2 km BSL in the beginning of the 92 eruption to ~3 km BSL post-eruptive period using co-eruptive deformation derived from InSAR 93 data. Freymueller and Kaufman (2010) interpreted the magma source as a Mogi sphere lying 94 95 ~1.9 BSL and captured the reinflation almost three weeks right after the vigorous ash emissions.

Subsequent to the 2008 eruption, Qu et al. (2015) analyzed post-eruptive InSAR data from four satellite tracks and found a time varying inflating rate of 48-130 mm/yr from 2008 to 2014 and found the best fit source accounting for this uplift signal is a Mogi source ~3.9 km BSL. However, using the same results, Xue et al. (2020) found a best fit model consisting of a Mogi source at ~3.2 km lying beneath a shallow sill at about 0.9 km, they then updated the magma accumulation status of Okmok using campaign and continuous GPS data with the source derived using the InSAR results from Qu et al. (2015). In this study, we focus on the posteruptive deformation from 2008 right after the eruption to 2020.

In this paper, we use PSInSAR techniques to produce deformation time series for Okmok volcano, using data from 4 different sensors and six independent imaging geometries to track the evolution of the Okmok magma system since its 2008 eruption. The deformation time series capture the temporal evolution of the surface deformation at Okmok volcano. The Ensemble Kalman Filter (EnKF) is used to track the source parameters over time as the system evolves. EnKF is a time-dependent inversion filter based upon the traditional Kalman Filter (KF). The KF is a data assimilation algorithm that evaluates a linearly evolving system problem. It uses a series of measurements observed over time containing statistic noise and other inaccuracies to produce estimates of unknown model parameters (Kalman, 1960). The EnKF uses an ensemble of forward models to link system parameters to observations. The ensemble approach enables EnKF to overcome the limitations of the traditional KF and Extended Kalman Filter (EKF), such as high computation load and poor performance when dealing with highly nonlinear systems (Evensen, 2003, 2009). Here we adopt the framework developed by Gregg and Pettijohn (2016) and Zhan and Gregg (2017) to assimilate the deformation time series computed from InSAR into linear elastic Finite Element Models (FEM) of the magma source to investigate the evolving state of the Okmok magma system.

96

97 98

99

100101

102

103

104

105

106

107

108109

110

111112

113

114

115

116

117

2 Methods and Datasets

2.1 Time-series InSAR algorithms

122123124

125

126

127

128129

130

131

132

133

134

135

136137

138

139

140141

142

143

144

157

145

146

147

148

149

150

151

152

158

160

161

162

121

Conventional InSAR deals with only a few interferometric pairs. In this scenario, the measurement accuracy can be significantly compromised by artifacts and noise such as Atmospheric Phase Screen (APS) due to the atmospheric phase delay, orbital error introduced by inaccurate satellite orbit determination, unwrapping errors due to large phase jump or decorrelation, topography error due to inaccurate DEM, and geometric errors associated with the change in look angle between the sensor and the ground targets (Hooper et al., 2007a). The PSInSAR technique provides a way of approaching such problems, PSInSAR algorithms aim at extracting scattering mechanisms from ground targets that persist over the observation period to maintain good interferometric coherence. Since the emergence of Persistent Scatterers (PS) concepts in the last two decades, there are two main approaches for PSInSAR implementation. One approach uses the amplitude dispersion as a proxy for the stability of the scattering mechanism; points with small amplitude dispersions are selected and used for subsequent PSInSAR processing (Ferretti et al 2001). The other one assumes the noises are spatially uncorrelated and identifies PS by noise level thresholding (Hooper et al., 2004; Hooper, 2008). In this research, we use the later one, which is also referred to as the Stanford Method for Persistent Scatterers (StaMPS). The standard procedure of PS incorporating SBAS, hereafter called PS-SBAS, is used to process the SLC image stack. We will briefly describe the algorithm below, and for technique details, readers should refer to Hooper et al. (2007a) and Hooper (2008).

During the StaMPS processing, the wrapped interferometric phases are assumed to contain both spatially correlated and uncorrelated parts:

$$\Delta \Phi = \Delta \Phi_{\text{def}} + \Delta \Phi_{\text{atm}} + \Delta \Phi_{\text{orb}} + \Delta \Phi_{\text{topo}} + \Delta \Phi_{\text{noise}}, (1)$$

where $\Delta\Phi_{def}$ is the spatial-correlated deformation, $\Delta\Phi_{atm}$ is the spatially correlated APS, $\Delta\Phi_{topo}$ is the spatially uncorrelated DEM error, $\Delta\Phi_{noise}$ is the spatially uncorrelated noise term due to variability in scattering within the pixel, thermal noise and coregistration errors (Hooper et al 2004).

To evaluate the noise level, the spatially uncorrelated terms are first filtered out using a Combined Lowpass and Adaptive Filter (CLAP), the DEM error is then estimated in a least-squares sense. After the subtraction of the DEM error term from the spatially uncorrelated signal, a measure of phase temporal stability can then be computed as

$$\gamma = \frac{1}{N} \sum_{i=1}^{N} \exp \{j(\Delta \Phi_{SUC,i} - \Delta \widetilde{\Phi}_{topo,i})\}, (2)$$

- where N is the number of interferograms, $\Delta\Phi_{SUC,i}$ is the spatial uncorrelated term estimated
- from the CLAP of each interferogram, $\Delta\Phi_{\text{topo,i}}$ is the estimated DEM error for each time step.
- After PS selection using a stochastic scheme and noisy PS candidates weeding, the wrapped
- interferograms are unwrapped with a 3D unwrapping algorithm (Hooper et al., 2007b).

2.2 SAR datasets and processing

SAR datasets used in this study begin in September 2008, one month after the last ash emissions recorded on August 20, 2008. The C-band Envisat P222 track spans from 2008 to 2010 with 7 scenes in total. The TerraSAR-X P116 track spans from 2011 to 2014 with 8 scenes

164

165

166

167

168

169

170

171

172

173

174

175

176

177

178

179

180

181

182

183

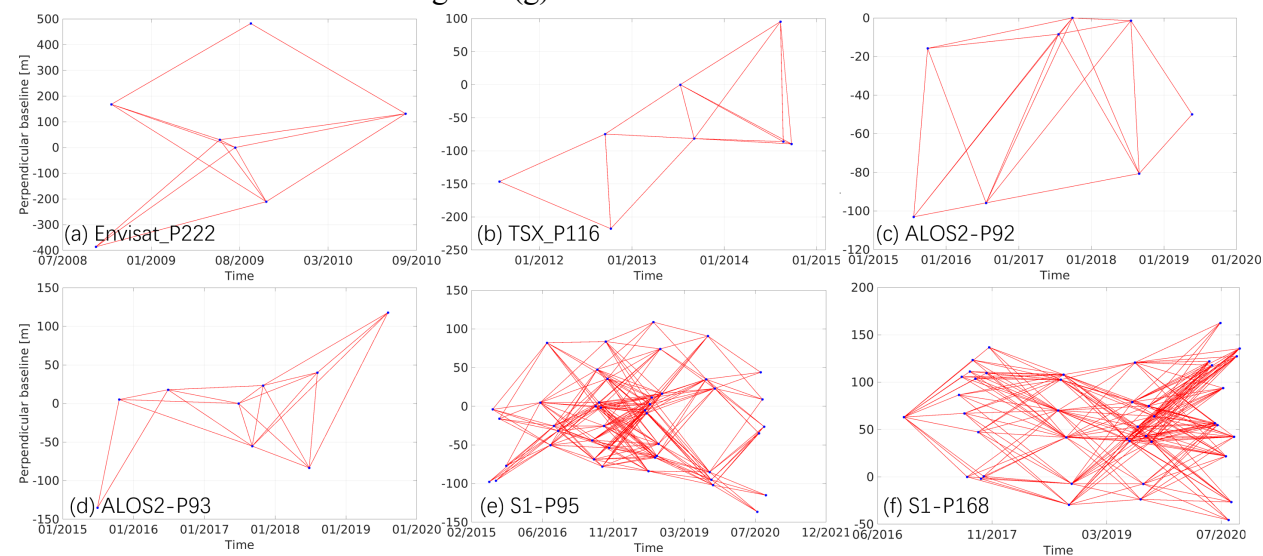
184

185

186

in total. The temporal gap is about 11 months between the Envisat and TerraSAR-X and about 9 months between the Sentinenl-1 and TerraSAR-X. The C-band Sentinel-1 P95 track spans from 2015 to 2020 with 44 scenes, and P168 track from 2016 to 2020 with 40 scenes. The L-band ALOS-2 P92 track spans from 2015 to 2019 with 8 scenes, and P93 track from 2015 to 2019 with 9 scenes. All of the SAR images are acquired in summer from June to October. Winter scenes are discarded due to the decorrelation effects introduced by the thick snow and ice coverage. To remove the topographic contribution from the interferometric phase, we use the high-resolution ArcticDEM generated with optical stereo imagery (Porter et al., 2018). Precise DORIS orbits are used for the Envisat data for baseline calculation. Interferometric pairs with relatively small perpendicular baseline and temporal separation are selected to reduce the spatial and temporal decorrelation. Additionally, to reduce the influence of APS to the 3D phase unwrapping, a minimum temporal separation of 60 days is used when smoothing the phase spatial gradient in time for computation of the cost function for the network-flow phase unwrapping. The perpendicular baselines threshold given to each track is a compromise between relatively denser network for retrieving single referenced deformation history and relatively smaller perpendicular baseline to maintain interferometric coherence. The reference region for phase unwrapping is selected in either the southeast area near the CGPS station OKFG, or the northeast of the island if OKFG is not covered in the SAR images. The volcanic deformation over these regions are negligible.

The SBAS networks constructed are shown provided in Figure 2. The derived deformation time series are then validated with the (CGPS) data provided by the Nevada Geodetic Laboratory (Blewitt et al., 2018) from 3 sites: OKCE, OKNC and OKSO (Figure 1). The temporal coverage of CGPS data are shown as in Figure 2(g).



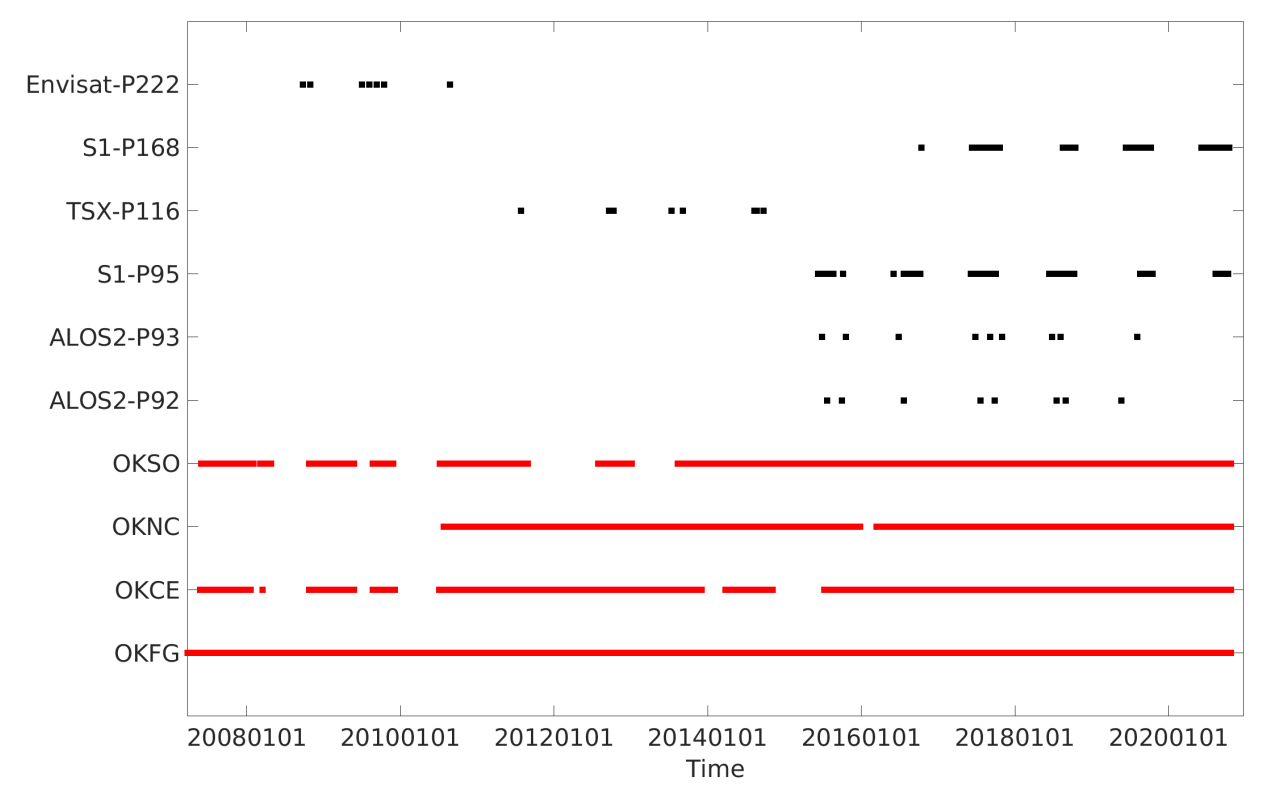


Figure 2. Temporal-spatial baseline distribution of the SBAS network for the six InSAR datasets and temporal coverage of GPS data used: Interferograms with perpendicular baseline less than (a) 400 m for C-band Envisat P222 track; (b) 200 m for X-band TerraSAR-X P116 track; (c) 100 m for L-band ALOS-2 P92 track; (d) 200 m for L-band ALOS-2 P93 track; (e) 150 m for C-band Sentinel-1 P95 track; (f) 100 m for Sentinel-1 P168 track. (g) Temporal coverage of SAR and Continuous GPS (CGPS) data used in this paper.

2.3 Time-dependent source inversion

The deformation time series calculated with PSInSAR are then used for the inversion of the Okmok magma source with an ensemble of FEMs updated by the EnKF. We use a three-dimensional, linear elastic FEM to model stress and strain with COMSOL Multiphysics 5.5 \mathbb{R} . The source is modeled as an incompressible pressure sphere with a radius of R and an overpressure ΔP (figure S1), embedded at a depth of Z below the surface. The host rocks are modeled as a block of homogeneous linear elastic materials with a dimension of $60 \ km \times 60 \ km \times 20 \ km$, a Young's modulus of $7.5 \times 10^{10} \ Pa$ and a Possion's ratio of 0.25. Initial isostatic stress is applied in response to the constant gravity ($g = 9.8 \ m^2/s$).

 $\sigma_1 = \sigma_2 = \sigma_3 = \rho g z$, (3)

Where σ_i are the initial principle stress, $\rho = 2700 \ kg/m^3$ is the density of the crust, z is the depth. The side and bottom boundaries are characterized by roller condition and the upper surface is free to deform. We use a mesh-controlled domain with finer mesh grids near the magma reservoir location for higher accuracy.

The EnKF formulation is constructed by replacing the calculation of Jacobian of the transformation model from system parameters to observations with model ensembles. Combining model predictions from previous time step with observations, the evolutions of the

system parameters are tracked using a Markov Chain of Monte Carlo (MCMC) method (Evensen, 2003):

$$A^{a} = A + P_{e}H^{T}(HP_{e}H^{T} + R_{e})^{-1}(D - HA), \quad (4)$$

where A is the forecast ensemble matrix of the system parameter to be estimated and predicted observations, P_e is the covariance matrix of A, H is the maping matrix that linking the forcast ensemble A to the observations, R_e is the covariance matrix of the observations and D is the matrix of measurements.

For the EnKF setup, an iterative parameter updating strategy is employed as described in Zhan and Gregg (2017). 100 ensembles are used and a maximum of 10 iteration steps to balance between parameter precision and computational costs. Previous studies suggest better inversion results could be achieved when displacements from both InSAR and GPS measurements are jointly assimilated into the sequential source inversion (Zhan and Gregg, 2017; Albright et al., 2019). However, for our case, the three CGPS records do not provide enough constraints to the source parameters, i.e., three-dimensional location, magma reservoir radius and overpressure inside the magma chamber. Assimilation of GPS data leads to divergence instead of providing important time evolution updates during the temporal gap of InSAR data collections. Moreover, since the InSAR data from different tracks take different references, and only the TerraSAR-X are acquired from a descending orbit, it is not feasible to assimilate InSAR observations from different tracks. In such scenario, we conduct the time dependent source inversion independently for each InSAR tracks and then link them with the CGPS data to provide the full-time range of the magma system evolution of Okmok after the 2008 eruption. The GPS data were downsampled to 30-day average bins. The source locations for the CGPS inversion are fixed based on our InSAR results. Only the source strength, i.e., radius of the pressure sphere and over pressure inside the chamber are variables that updated at each EnKF updating step. The cumulative post-eruptive volume changes at each InSAR reference date are also estimated from the CGPS records. The cumulative volume changes associated with the InSAR observations are then derived by adding the incremental volume change from each track to the cumulative volume change at the reference date. To reduce the influence of APS and other noise to the source modeling, we only use InSAR results inside the caldera, which we will discuss in detail later.

3 Deformation history and source evolution

3.1 Deformation history since 2008

212

213

240

214

215

216

217

218

219

220

221

222

223

224

225

226

227

228

229

230

231

232

233234

235

236

237

238

239

241

242243

244

245

246

247

248

249

250

251252

253

254

255

The deformation history since the 2008 eruption is generated with the PSInSAR algorithms, with Spatially Correlated Look Angle (SCLA) error corrected using a least-squares sense. APS correction in StaMPS is accomplished by a high-pass filter in time and low-pass filter in space (Hooper et al., 2004). For this application, SCLA correction alone is enough for accurate deformation mapping inside the caldera (Figure 4). Results with APS correction tend to bias deformation signals both inside and outside the caldera compared to the records of CGPS, which we use as ground truth to validate the InSAR measurements. One possible reason may be that the inflation rates are time varying, the low-pass filter during APS correction tends to flatten the higher frequency signals and introduce bias. Therefore, APS corrections are not applied in the InSAR results. After the SCLA correction, the cumulative deformations are derived from the SBAS network using a least-squares approach. The deformation mapped from different datasets are shown as in Figure 3, and more detailed deformation time series can be found in figure S2. The corresponding cumulative deformation derived from each SAR dataset is shown in table 1.

The inflation is persistent throughout the whole observation period from 2008 to 2020 for all the six InSAR tracks. The region of most deforming area is located near the center of the caldera, with little variation during the entire time span.

Scene ID	Envisat P222	TerraSAR-X 116	ALOS-2 P92	ALOS-2 P93	Sentinel-1 P95	Sentinel-1 P168
Start time	20080924	20110727	20150722	20150629	20150609	20161012
End time	20100825	20140924	20190522	20190805	20201010	20201015
Cumulative deformation (mm)	300	180	280	310	350	320

Table 1. Cumulative deformation for each InSAR dataset. Dates are in the format of YYYYMMDD.

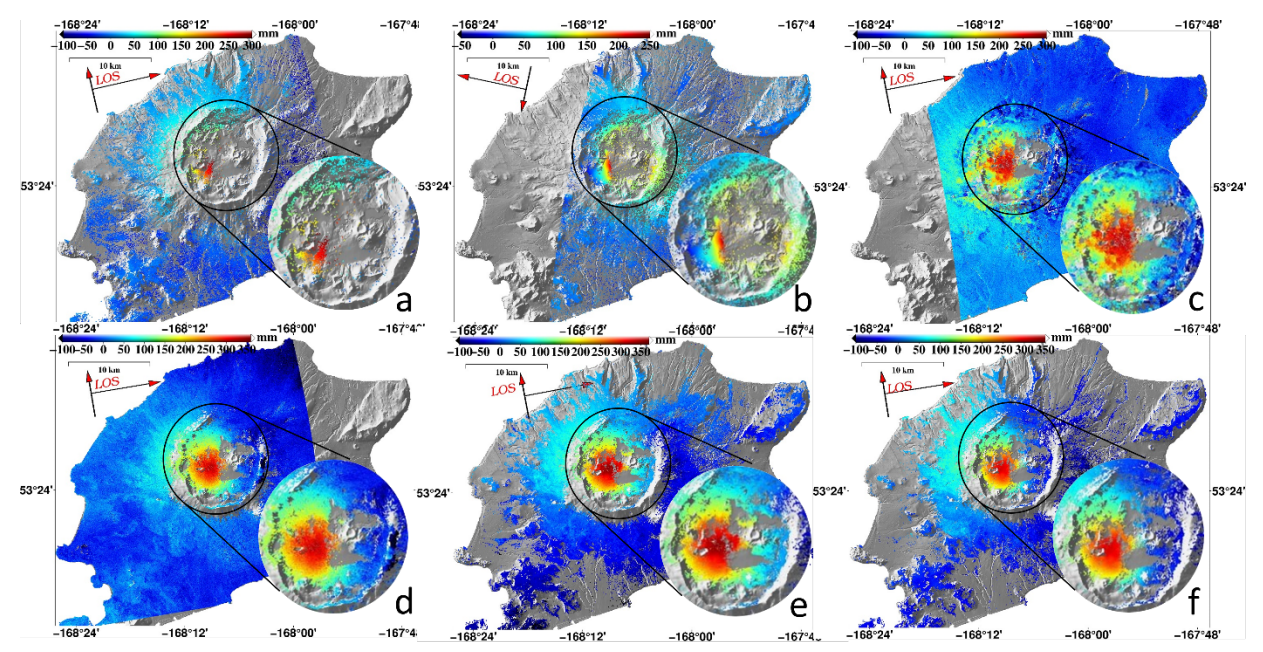


Figure 3. Cumulative deformation maps from different InSAR tracks. Signal in red corresponds to uplift. (a) Envisat P222 track, (b) TerraSAR-X P116 track, (c) ALOS-2 P92 track, (d) ALOS-2 P93 track, (e) Sentinel-1 P95, (f) Sentinel-1P168. All the deformation measurements are in the Line-Of-Sight (LOS) directions. Deformations inside the caldera are enlarged in the inset to improve visibility.

The cumulative deformation maps are then compared with the CGPS records for validation of measurement accuracy at three CGPS stations, i.e., OKCE, OKNC, OKSO (figure 4). The CGPS measurements are corrected for non-volcanic deformation, mainly tectonic signals due to the interaction between the Pacific plate and the North American plate, by subtracting the measurements from a CGPS station far away from the deforming center at a distance of about 15 km, i.e., OKFG (figure 1). The three-dimensional GPS measurements are then projected to the LOS direction of the corresponding SAR imaging geometry. PS within 100 meters of the CGPS sites are selected and their averages are computed for the comparison. The promising agreement between the InSAR derived deformation time series and the CGPS solution suggests our InSAR measurements are reliable, with most of the standard deviations of the difference between the InSAR results and CGPS records less than 1 cm.

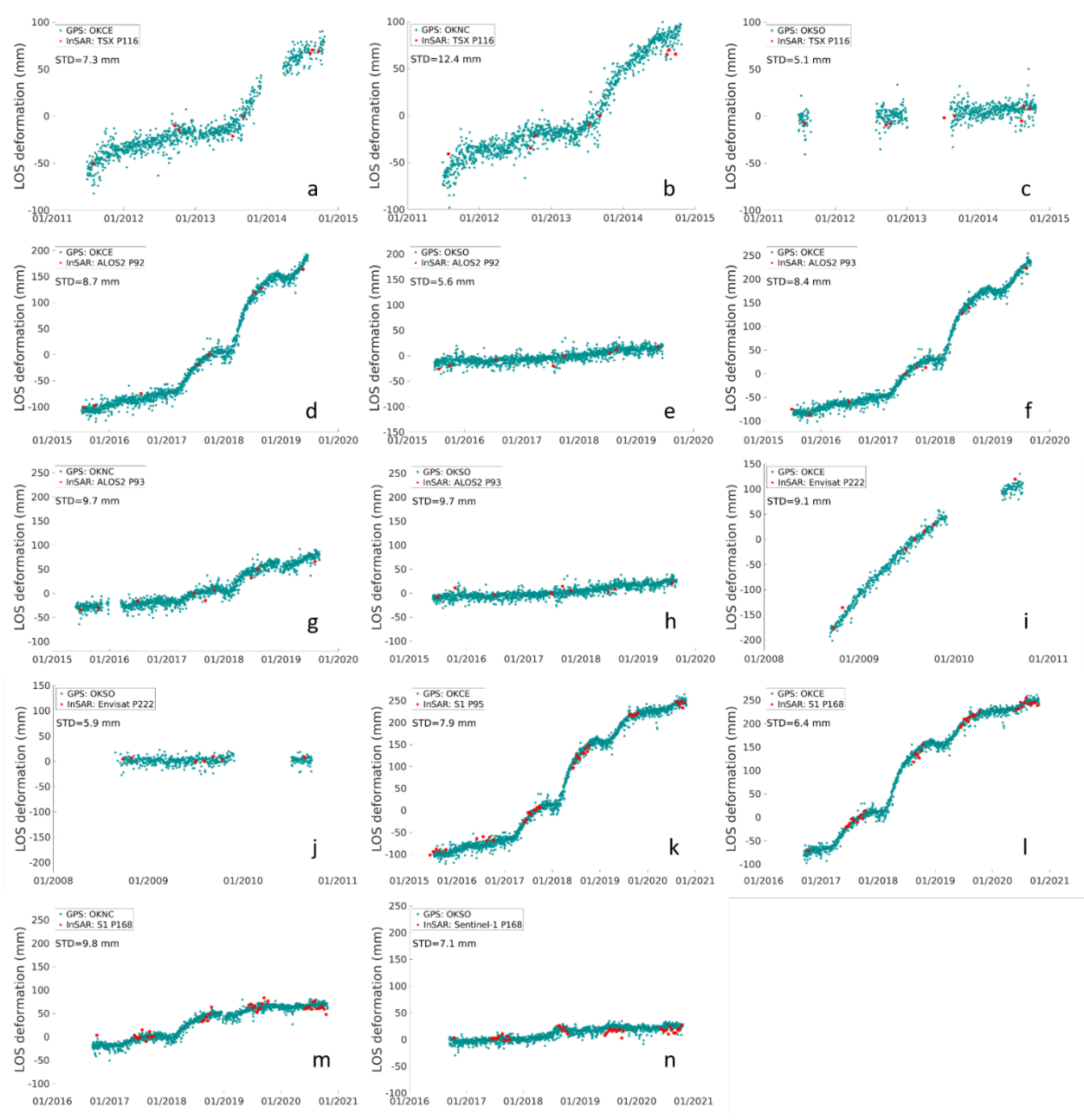


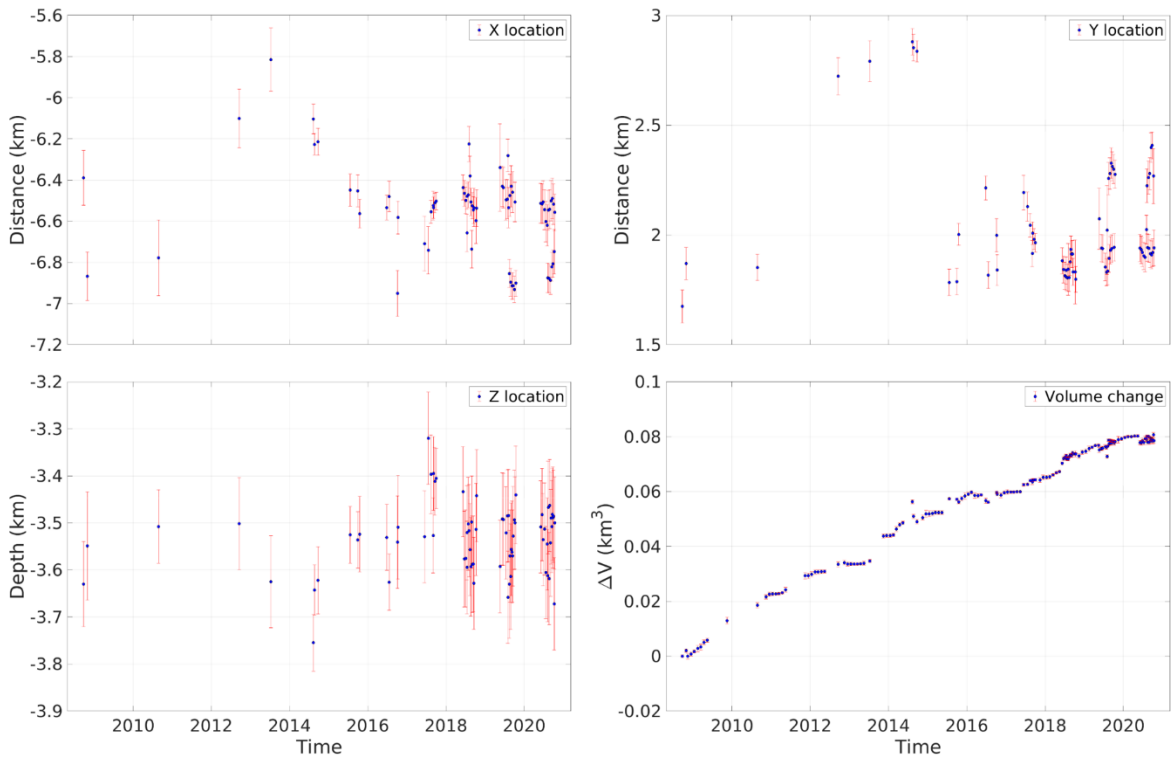
Figure 4. Comparison of deformation time series from InSAR with the CGPS observations in the LOS direction: (a) (b) (c): deformation from TerraSAR-X P116 track and GPS at station OKCE, OKNC and OKSO, respectively; (d) (e): deformation from ALOS-2 P92 and GPS site OKCE and OKSO, respectively; (f) (g) (h): deformation from ALOS-2 P93 and GPS site OKCE, OKNC and OKSO, respectively; (i) (j): deformation from Envisat P222 and GPS site OKCE and OKSO, respectively; (k): deformation from Sentinel-1 P95 and GPS site OKCE; (l) (m) (n): deformation from Sentinel-1 P168 and GPS site OKCE, OKNC and OKSO, respectively. All the GPS observations are referenced to OKFG and are shifted to the same reference data of the

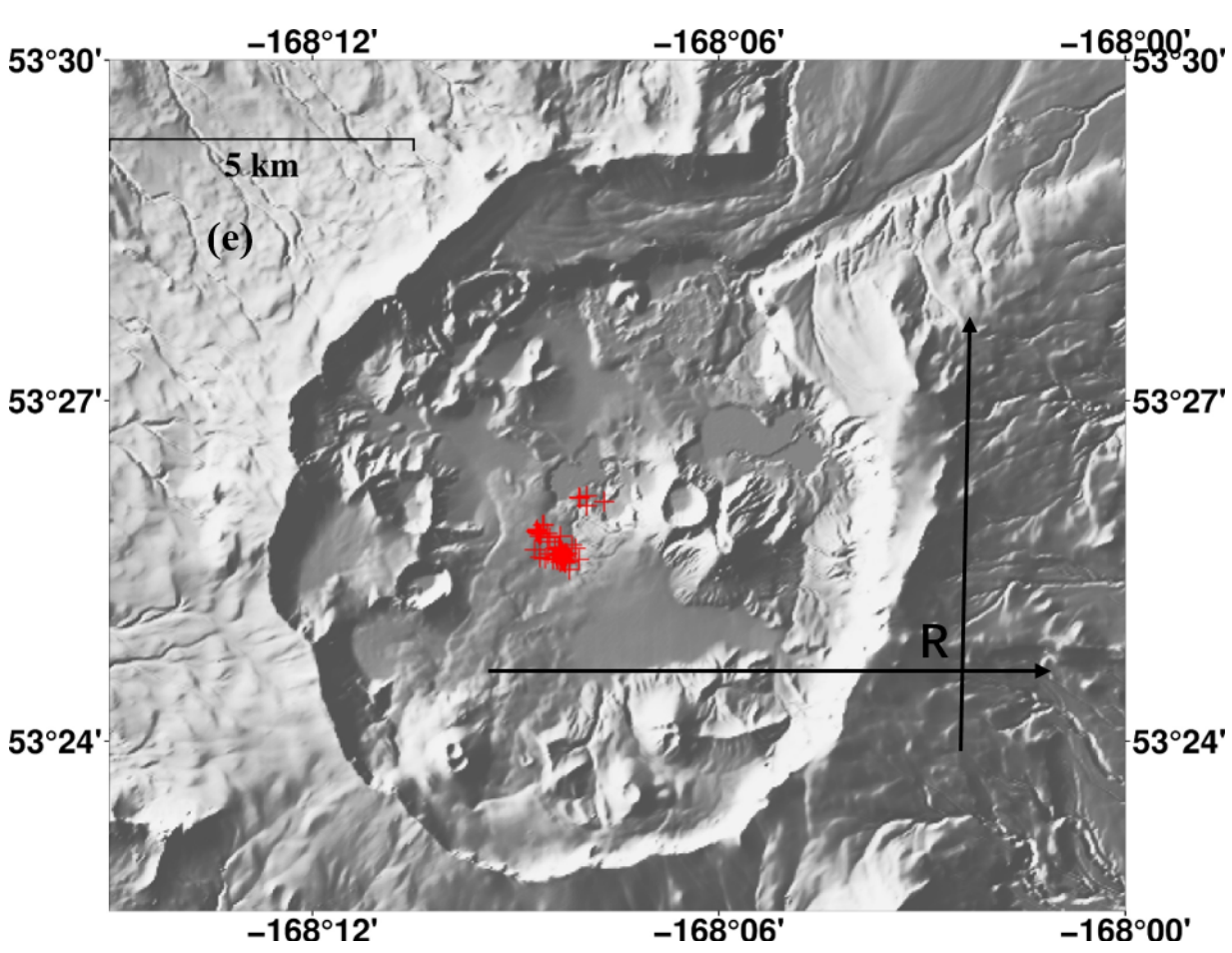
InSAR observations, respectively. The InSAR measurements agree well with the CGPS records with most of the standard deviation of their difference less than 1 cm.

3.2 Evolution of the magma system

We use a single incompressible pressure sphere to capture the temporal evolution of the deformation obtained above. The InSAR results are resampled to $50m \times 50m$ grids to reduce noise and data volume for the EnKF processing (figure S3). The measurement uncertainty of InSAR is determined as the standard deviation of the phase of PS fallen into the same grid, plus the uncertainties introduced by APS, which is computed using semi-variograms over areas where volcanic deformation is negligible (Murray et al., 2019). One great advantage of EnKF is not only the evolution of parameters are tracked with the time-dependent filter, the uncertainty of the system parameters can also be estimated to the first order for each assimilation (Evensen, 2009). In our case, the uncertainty is high for the first a few steps and then the estimation converges rapidly over time. Due to the nature of non-uniqueness in the inversion, we use a single volume change, which combines both the source radius and the overpressure of the magma chamber, to represent the source strength.

Our results show a stationary source embedded $\sim 3.5 \, km$ beneath the mean elevation of the caldera floor, which is equivalent to a source about 3 km BSL (Figure 5), can account for most of the observed InSAR signals and agree well with previous studies of the pre-2008 eruption magma system (Biggs et al., 2010; Fournier et al., 2009; Lu et al., 2005, 2010; Albright et al., 2019). The easting and northing of the source position are relatively unstable during 2008 to 2014 compared to those in the time period from 2015 to 2020, which was also identified in Qu et al (2015). As previous studies have confirmed that the position of the shallow magma source is stable without significant temporal variations, we believe that this fluctuation during 2008 to 2014 is a result of sparse spatial coverage of InSAR data inside the caldera, which adversely impacts the performance of EnKF leading to the need for a model spin-up period (Zhan and Gregg, 2017). Sparse PS density inside the caldera is caused primarily by the decorrelation associated with mobile tephra deposited during the 2008 eruption. Since after the 2008 eruption, magma storage in the source has been increasing at a time-varying rate with a maximum rate of about $0.006 \, km^3/yr$ during 2017 to 2018 and a minimum rate of about $0.003 \, km^3/yr$ during 2015 to 2016 and 2019 to 2020. The fluctuating magma accumulation rate is similar to that during the previous inter-eruption cycle during 1997 and 2008 (Lu and Dzurisin, 2014; Lu et al. 2010).





- Figure 5. Time dependent source models from 2008 to 2020 based on the InSAR data with error
- bars showing 1σ uncertainties. (a) Temporal evolution of easting coordinate of the magmatic
- deformation source with respect to an arbitrary reference R (figure 5 (e)) and its uncertainty. (b)
- Northing coordinate of the best-fit source as a function of time and its uncertainty. (c) Best-fit
- depth of the deformation source and its uncertainty as a function of time. (d) Evolution of source
- strength (cumulative volume change) and its uncertainty with time. (e) Lateral spreading of the
- inverted source position, where R is the reference point for the easting and northing coordinates.

4. Discussion

333

334

335

336

337

338

339

340

341

342

343

344

345

346347

348

349350

351

352

353

354

355356

357

358

359

360

361

362

368

363

364

365

366

367

4.1 InSAR processing error analysis

In this study, we use only the InSAR observations inside the caldera for the source inversion despite the fact that significant volcanic deformation can be easily identified at a distance of several kilometers away from the inflation center. This data selection strategy, which produced a rather persistent and precise estimation of the magma system (Figure 5a, 5b, 5c, 5e), is an optimization for the derived time-series InSAR results. The methodology we use for the multiinterferogram algorithm, PS-SBAS, is a three-dimensional algorithm which takes advantage of both the spatial and temporal information during the processing (e.g., the CLAP filtering conducted spatially on pixels in each data layer), and the linear regression of the look angle error done on pixels in time. In addition, manipulation of the three-dimensional information can improve the PS-SBAS performance significantly especially in presence of noise. For example, the 3D phase unwrapping algorithm in StaMPS uses a temporal and spatial smoothing to the spatial gradients of the nodes to derive the cost function for the statistic-cost network-flow phase unwrapping, which performs well especially when some SLC scenes are saturated with random noise. Nevertheless, in the presence of strong APS effects, the temporal smoothing may bias the estimation, and thus results in a systematically deviated unwrapped phase, which is the case for the PS-SBAS processing for Okmok.

Following the algorithms used in StaMPS, we employ the minimum standard deviation of the arc noise of each node as a representation of the noise for the computation nodes (Figure S6). The noise level around the inflation center inside the caldera is significantly lower than that outside the caldera for all the datasets except for the C-band Envisat, which is caused predominantly by the larger decorrelation effects associated with larger spatial baselines. Although the noise level is low for a considerable portion of areas away from the deformation center, the error can be cumulative in space and time using the network-approach phase unwrapping algorithm. Considering the noise level over the caldera rim is significantly high and our measurements near the locus is reliable (Figure 4), the measurement uncertainty in areas away from the center caldera can be large. After the 3D phase unwrapping, the cumulative deformation is derived from the SBAS network in a least-square scenario. We use a simple estimator ρ to evaluate the SBAS processing noise:

$$\rho = \sum_{i=1}^{N} \left(\left| \frac{\phi_{sb}^{i} - \phi_{sb_sim}^{i}}{\phi_{sb_sim}^{i}} \right| \cdot \frac{|\phi_{sb_sim}^{i}|}{\sum_{i=1}^{N} |\phi_{sb_sim}^{i}|} \right), \quad (5)$$

where ϕ_{sb}^i is the i_{th} out of N unwrapped interferogram in the SBAS network, $\phi_{sb_sim}^i$ is the i_{th} unwrapped interferogram calculated from the inverted single-referenced cumulative deformation map. ρ estimates the deviations of the unwrapped phase for each PS. Compared with the one derived from linear regression, ρ can be considered as a biased estimation of the signal to noise ratio (SNR) since $\phi_{sb_sim}^i$ is just a biased estimate to the real cumulative displacements. A large ρ indicates a larger uncertainty in

the unwrapped phase. Figure S7 illustrates the calculated ρ for each dataset. It is obvious that the noise level outside the caldera is significantly higher than that near the deformation locus for all the six InSAR tracks. The low ρ values in most area of the caldera suggest precise observations during the whole observation period. On the other hand, the good agreement between the InSAR data and CGPS records, especially the one located close to the deformation center, i.e., OKCE, suggests that our InSAR results have captured the temporal evolution of the deformation quite well and the derived displacements near the locus are reliable (figure 4). Outside the caldera, the volcanic deformation extends to a distance of several kilometers from the source to the volcano flank. The high ρ values in these areas indicate a rather wide distribution of points during the SBAS linear regression. Such results are still useful for the source inversion, if the overall effects of the individual deviation are negligible. However, since the APS effects are spatially correlated in each interferograms and is not temporally independent as discussed before, the APS artifacts in a single scene are not normally distributed and can be a catastrophe for determining the source parameters. For this reason, we have discarded signals outside the caldera to get a more persistent and accurate estimation of the deformation source.

Use of only deformation inside the caldera is verified for the Sentinel-1 P168 dataset. Source modeling is applied to both the full scene and the signal inside the caldera. The source parameters derived with signal inside the caldera are mostly consistent with the ones derived from the full scenes (figure S5) with only small deviations, indicating that the deformation inside the 10-km-wide caldera alone is enough to constrain the magma system. The inverted magma source models agree well with the previous studies before the 2008 eruption, especially with the previously InSAR derived models (e.g., Lu et al. 2005, 2010)). Our results indicate the source accounting for the post-eruptive deformation of Okmok since the 2008 eruption is still the same source which is responsible for the 1997 and 2008 eruptions and during the inter-eruption interval. The APS and decorrelation have always been a problem for modeling the magma source of Okmok over the Aleutian arc (Gong et al., 2015), our work in this paper may also provide some insights to the source modeling with time series InSAR data over areas with dense APS artifacts and decorrelation.

4.2 The stationary magma reservoir of Okmok

Using spaceborne SAR images acquired from six different imaging geometries at three frequency bands during 2008 to 2020 we have investigated the post-eruptive deformation of Okmok after the 2008 eruption. The produced deformation history shows that the Okmok started rapid reinflation with a persistent deformation rate of about 150 mm/yr within the first two years after the 2008 eruption, then slowed down to about 50 mm/yr during 2011 to 2013 and accelerated to about 90 mm/yr again during 2013 to 2014. The volcanic deformation rate was relatively steady from mid-2015 to about mid 2016 with a rate of about 50 mm/yr. From 2017 to mid 2019, the inflation rate increased again, with an average rate reached about 100 mm/yr. Since mid 2019, the inflation rate decreased again to about 40 mm/yr. The episodic pulse of inflation at different rate (figure 6) resembles those of the pre- and inter-eruption deformation patterns of the 2008 and 1997 events of Okmok, which inflate periodically at time-varying rates with exponential patterns and were interpreted as responses to the magma accumulation in the shallow reservoir about 3 km BSL (Lu et al., 2005, 2010a; Biggs et al., 2010). One major difference of the post-eruptive deformation after 2008 is that there is no period of guiescence as that during 1993-1996 and 2004-2007, which was interpreted as a critical state of pressurization for the reservoir where the surrounding hosting rocks are strong enough to temporarily retard the magma supply from depth (Lu et al., 2010a). This persistent inflation pattern at a time-varying rate suggests a persistent pressure gradient between the deep magma source and the shallow reservoir and a critical capacity of the magma reservoir beyond which the reservoir wall can no longer deform to accommodate the magma pressure has not yet reached since the 2008 eruption.

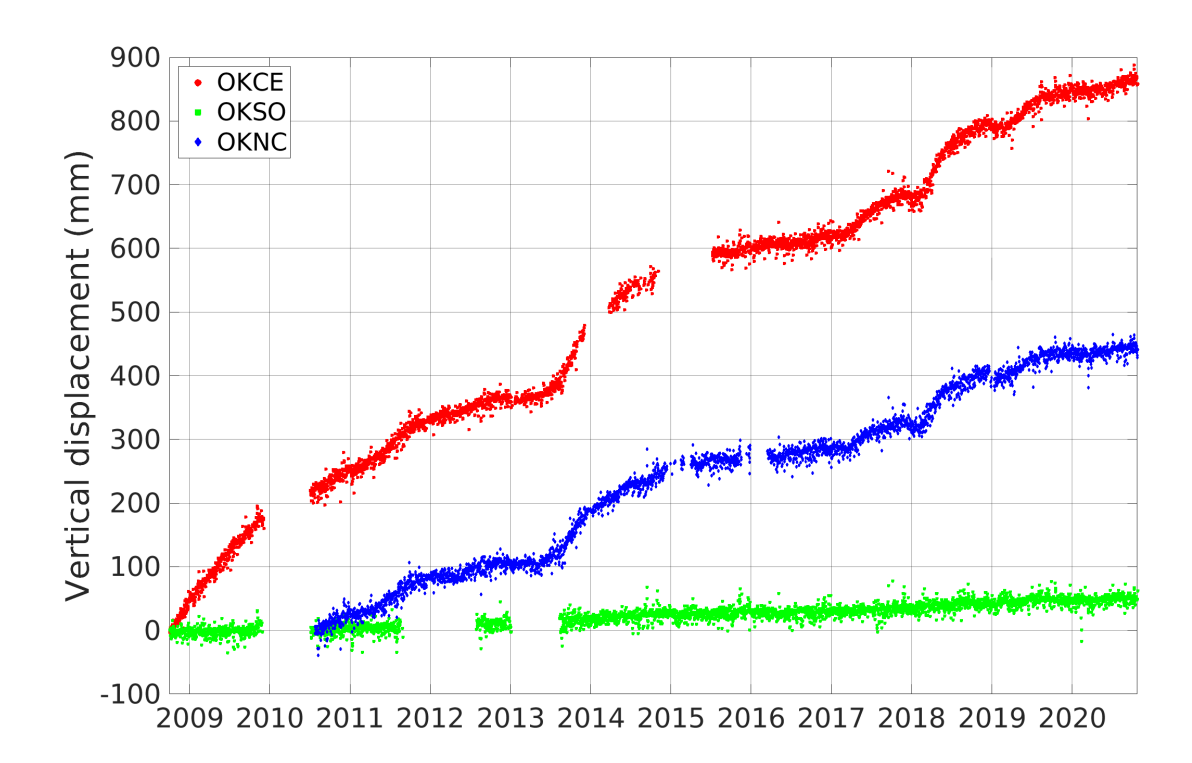


Figure 6. Vertical displacement of OKCE, OKSO from 2008 to 2020 and OKNC from 2010 to 2020. Clear episodic pulses of inflation can be seen from OKCE and OKNC.

418

419

420

421

422

423

424

425

426

427 428

429

430

431

432

433

434

435 436

437

438

439

440

441

442

The episodic pulse of inflation at different rate is especially evident in the vertical components of the CGPS records (figure 6). About five pulses of rapid inflation that slow down exponentially can be identified from the vertical CGPS records. The time varying inflation rates of a single pulse that decay exponentially in a single pulse can be possibly explained by a model where the shallow reservoir is fed by the magma flow from a deep source to compensate the pressure gradient (e.g., Lu et al., 2010; Lu et al., 2003b). The episodic pulses may indicate that the pressure balance between the shallow reservoir and the deep source were broken at the end of the previous pulse. Several volcanic processes can produce this kind of pressure gradient behavior. First, injection of hot magma into the relatively colder reservoir is accompanied with crystallization, during which the hot melts cool down and contract. The decrease in volume will result in increased pressure gradient between the shallow magma reservoir and deep magma source. However, the time scale of crystallization is generally much larger than the period of the episodic inflation (Caricchi et al., 2014), thus it cannot be solely responsible for the observed inflation pattern at Okmok. Degassing of excess volatiles from the cooling and crystallization of water-saturated magma may also contribute to the pressure decrease in the magma reservoir. Gas bubbles exsolve from the volatile-rich magma during crystallization, and the crystals tend to trap the gas bubbles. When the host rocks become permeable, gas can be expelled from the reservoir, which will result in pressure decrease in the reservoir. Another alternative explanation is that the pressure in the deep magma source might not be constant over time. The pressure in the deep source may increase episodically, which builds up episodic pressure gradient between the reservoir and the magma source and produces an episodic inflation pattern at Okmok. Similar episodic inflations have also been observed at other volcanoes, some of these cases were interpreted using a temporal blockage in the magma migration pathway (Cervelli and Miklius,

2003). A transient interruption of magma supply may be caused by a short-lived blockage, which is believed to be produced by the convective overturns of the degassed crystallized magma in the reservoir. The denser magmas move downward and tend to impede the magma flow from the pathway to the shallow reservoir. Upon removal, another episode of inflation begins. Whether these processes can occur in the magma system is still unknown, further investigations are still needed to test these hypotheses.

As mentioned above, spatially correlated APS effects are prone to saturate the InSAR results outside the caldera and compromise the source inversion significantly, especially when the APS can reach a magnitude comparable to the deformation signal. In our case, the signals outside the caldera with dense APS are masked out, and the deformation time series are modeled with numerical finite element models and a best fit magma source is found located at about 3.5 km beneath the caldera floor, which agrees well with the previous studies (Lu et al., 2005, 2010a; Biggs et al., 2010), suggesting the same magma source accounting for the progressive pre- and inter-eruptive deformation of the 1997 and 2008 eruption. Ou et al. (2015) mapped the posteruptive deformation during 2008 to 2014 and found a Mogi source embedded about 4 km beneath the caldera center, which is about 1 km deeper than previous studies conducted with InSAR. Using the same datasets, Xue et al. (2020) identified significant deviations between the GPS and InSAR results inside the caldera near the locus and interpreted them as localized deformation possibly related to self-compaction and erosion of new tephra by the 2008 erosion and viscoelastic relaxation and thermo-elastic cooling from older lava flows. After masking the signals inside the caldera where the InSAR and GPS are not compatible and combined with GPS records, a Mogi source located about 3.2 km together with a shallow sill was used to account for the post-eruptive deformation. However, we have recomputed the deformation history during 2008 to 2014 with the same datasets (i.e., the C-band Envisat P222 and X-band TerraSAR-X P116 track) using the PSInSAR processing procedure deployed in this study, and found good agreements between the InSAR and GPS. Also, results from C-band Sentinel-1 and L-band ALOS-2 show little deviation to the CGPS records since 2015, indicating that our mapped deformation inside the caldera is accurate for the source inversion. The source depth accounting for the inflation immediately after the 2008 eruption in our study is very close to that before 2008, which is consistent with the progressive deepening in the deflation source during the 2008 eruption in previous inter-eruption observations by Lu et al. (2010b) and Freymueller et al. (2010), indicating magma accumulation inside the shallow reservoir resumed rapidly after the eruption. The inferred locations of the magma reservoir from InSAR coincides with the low seismic velocity zone inferred from seismic radial anisotropy and resistivity survey (Miller et al., 2020).

4.3 Erosion of the 2008 tephra deposits

443

444

445

446

447

448

449

450

451

452

453

454

455

456

457

458

459

460

461

462

463

464

465

466

467

468

469

470

471

472

473

474 475

476

477 478

479

480

481

482

483

484

485

486

487

488

Although the erosion of the unconsolidated tephra deposits cannot be mapped directly, our InSAR results can still provide some insights into it. Since the 2008 eruption, the dense volcanic sediments inside the caldera have become a pervasive and insurmountable problem for deformation mapping with InSAR. Rapid surface changes associated with erosion of the deposits would degrade the interferometric coherence. For the identification of PS using SAR datasets with small perpendicular baselines, the spatial coverage of PS represents basically the area without significant temporal changes. Our InSAR observations cover only a small portion inside the caldera and no coherent measurements can be obtained near Cone D (figure 3), which produced the 2008 phreatomagmatic eruption and is deposited with tephra to a thickness of 25-

50 meters (Larsen et al., 2015). The PS coverage of the C-band Envisat P222 right after the 2008 eruption is less than that of the X-band TerraSAR-X which started about two years after the eruption. Considering that the decorrelation associated with surface erosion is stronger for the X-band sensor (e.g., Wei et al., 2009; Hanssen, 2001), our results indicate that the erosion and consolidation of the tephra materials evolved rapidly in the first two years after the eruption. Also, the spatial extent of PS in the C-band Sentinel-1 or L-band ALOS-2 covers most of the caldera area except for the region near cone D and water bodies in the east caldera, suggests that large scale of sediment erosion that reshaped the surface rapidly after the 2008 eruption has ceased in these areas since 2015.

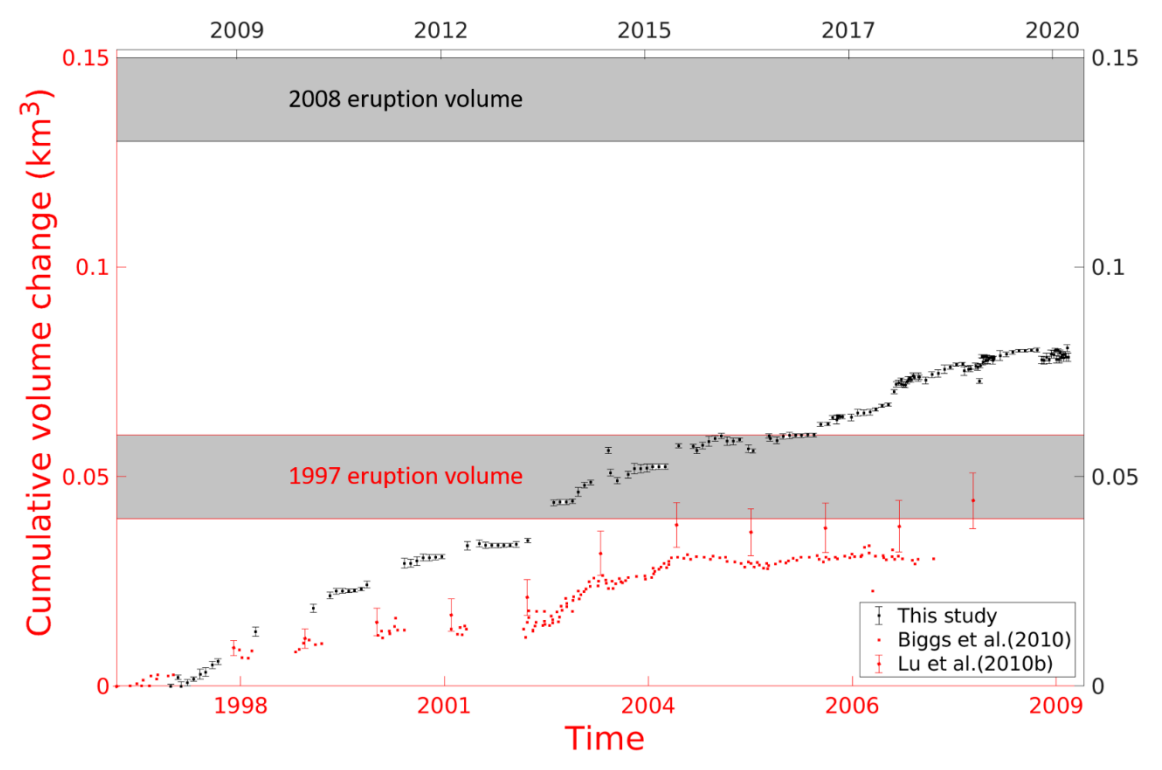


Figure 7. Comparison of the cumulative volume change since 2008 with that during 1997 to 2008. The 1997 eruption volume is from Lu et al. (2005), the 2008 eruption volume is the coeruptive volume change from Lu and Dzurisin (2014). The data in this study are plotted with respect to the axes on the top and the right; the volume changes from 1997 to 2008 from Biggs et al. (2010) and Lu et al. (2010b) are plotted with respect to the axes on the bottom and the left.

4.4 Magma supply dynamics

The InSAR deformation history can be well modeled by a simple spherical pressure source which is relatively stationary through time and is consistent with the calculated pressure source prior to the 2008 eruption. Lu et al. (2010b) suggests a shallow contracting sill at a depth ~ 0.5 km during the 2008 eruption and they interpreted this as the extraction of ground water which was responsible for the phreatic nature of the 2008 eruption. Freymueller et al. (2010) also detected changes in the magma source immediately before and during the 2008 eruption; they suggest that these variations are related to preexisting magma storage at shallower depths prior to 1997, with a more chemically evolved magma that accounts for the slightly higher SiO_2 content

and 2-3 times larger eruption volume. We cannot evaluate the possibility of the existence of such a shallower structure with only the coherent InSAR observations from 2008 to 2014 due to the lack of spatial coverage near the center of the caldera, where the shallow sill was thought to reside (Xue et al., 2020, Lu et al., 2010b). However, starting from 2015, the availability of Sentinel-1 and ALOS-2 data enables a larger spatial coverage than the Envisat and TerraSAR-X. We have detected no localized deformation that is indicative of shallower sources for this time range. Hence, the shallower sill structure discussed in Freymueller et al. (2010) and Lu et al. (2010b) was likely a transient process associated with the 2008 eruption.

514

515

516

517

518

519

520

521

522

523

524

525

526

527

528

529

530

531

532533

534

535

536

537

538

539

540

541

542

543

544

545546

547

548

549

550

551552

553

554

555

556

557

558

559

The 2008 eruption was significantly different from its predecessors. We compared the posteruptive magma accumulation with that during the inter-eruptive period from 1997 to 2008 (Figure 7). The rapid magma replenishment occurred immediately after the 1997 and the 2008 eruptions and both show episodic patterns with time-varying rates decaying exponentially. We notice that the magma intrusion rate after the 2008 eruption is almost three times of that after the 1997 eruption. Consider a conceptual model widely used for Okmok and other shield volcanoes in the Aleutian where the shallow reservoir is fed by the magma flow from a deep source to compensate the pressure gradient (e.g., Lu et al., 2010; Lu et al., 2003b). The much larger posteruption magma replenishment rate indicates a reduction in the resistance inside the magma transport pathway from the deep source to the shallow reservoir after the 2008 eruption, or that the pressure difference between the shallow reservoir and the deep source after the 2008 eruption is much higher than after the 1997 eruption. Whether and how the extrusion of magma in the shallow reservoir during the 2008 eruption can affect the deep magma migration pathway remains uncertain. We are inclined to suggest that the increase in the pressure difference following the 2008 eruption is the result of a pressure decrease in the shallow reservoir assuming the pressure in the deep magma source remains constant. Hence, the much higher inflation rate after the 2008 eruption may be the result of a larger pressure deficit in the shallow reservoir as the eruption volume from the 2008 eruption was much greater than that of the 1997 eruption. The cumulative volume change after the 2008 eruption also indicates a much higher magma accumulation rate; ~0.08 km³ of magma has been intruded into the shallow reservoir from 2008 until 2020, which is about twice the rate observed from 1997 to 2008. Along with the posteruptive surface deformation, which can be well determined by the spherical source, we speculate that the increase in the eruptive volume associated with the 2008 eruption relative to the prior historical eruptions from Cone A is likely resulted from over-extrusion of magma in the shallow reservoir during the 2008 eruption. The over-extrusion during the eruption thus causes a possible greater reduction in magma pressure compared to the 1997 eruption, which subsequently leads to a higher magma replenishment rate and large inflation rate.

The over-extrusion may be a result of a change in the mechanism of the magma ascent from the reservoir to the surface as discussed in Larsen et al. (2015), where the magma migration pathway changed from a single, narrow shallow conduit that connecting the reservoir with Cone A to a dike-fed system tapping a larger portion of the eruptible magma from storage. This is consistent with the inter- and co-eruptive seismicity distribution associated with the 2008 eruption (Ohlendorf et al., 2014). We infer that the two earthquake swarms located beneath Cone A and Cone D recorded during the time period from early 2003 to July 6 2008 and from 6 to 13 2008, respectively, are indicative of brittle failure associated with the magmatic fluid migration. The distinctly different event locations are evidence of different magma ascent pathways accounting for the 1997 and the 2008 eruptions. An alternative explanation involves the phreatomagmatic nature of the 2008 eruption. Lu et al. (2010a) identified minor deflations

during the inter-eruptive period from 2004 to 2005, which was associated with the outgassing of volatiles. Signals of localized deflation during the 2008 eruption were also identified and attributed as the withdrawal of ground water (Lu et al. 2010b). The exsolution of magmatic volatiles may fracture the host rocks of the spherical magma source and shallower ground water reservoir, making it possible for explosive interaction between the magma and the ground water, which further fracture the magma migration pathway and finally produced the explosive eruption and the significantly large eruption volume. A schematic illustrating the two hypotheses above is shown in figure 8.

560

561

562

563

564

565

566

567

568

569

570

571

572

573

574

575

576

577

578

579

580

581

582

583

584

585 586

587

The cumulative volume change inside the shallow reservoir until 2020 is about 60% of the total reservoir volume change during the 2008 eruption (~0.08 km³). The 2008 eruption occurred when the volume of magma withdraw during the 1997 eruption was almost replenished (Figure 7), which may imply that the triggering condition of an eruption is when the reservoir capacity is reached. In addition, declining inflation rates that last for a few years prior to the eruption and a period of oscillations including deflation and inflation may also serve as an indication that an eruption draws near (Fournier et al., 2009; Lu et al., 2010). Since 2019, the inflation rate at Okmok decreased to about $40 \, mm/vr$, which is the lowest since the 2008 eruption and is close to that during the pre-eruptive inflation during 1993 to 1995. Therefore, continuous monitoring ground deformation at Okmok volcano is critically important in the future. Even if surface deflation such as that observed during 2004 to 2005 were detected at Okmok, without knowledge of the magma pressure in the shallow reservoir and the deep source, it is difficult to determine whether the decreasing inflation rate is an indication of an imminent critical pressure state or just another tail of the exponential decaying magma replenishment cycle as those during 2011 to 2013 and 2015 to 2016. Limited by the over-simplified nature of the models we use, further understanding of the volcanic system can be achieved only when the realistic physical processes critical for the volcanic life cycles are considered, e.g., compressibility of the magma, melt viscosity, degassing and crystallization, which require assimilation of multi-disciplinary data such as tomography of the sub-caldera structure from seismology and magma evolution from geochemical research.

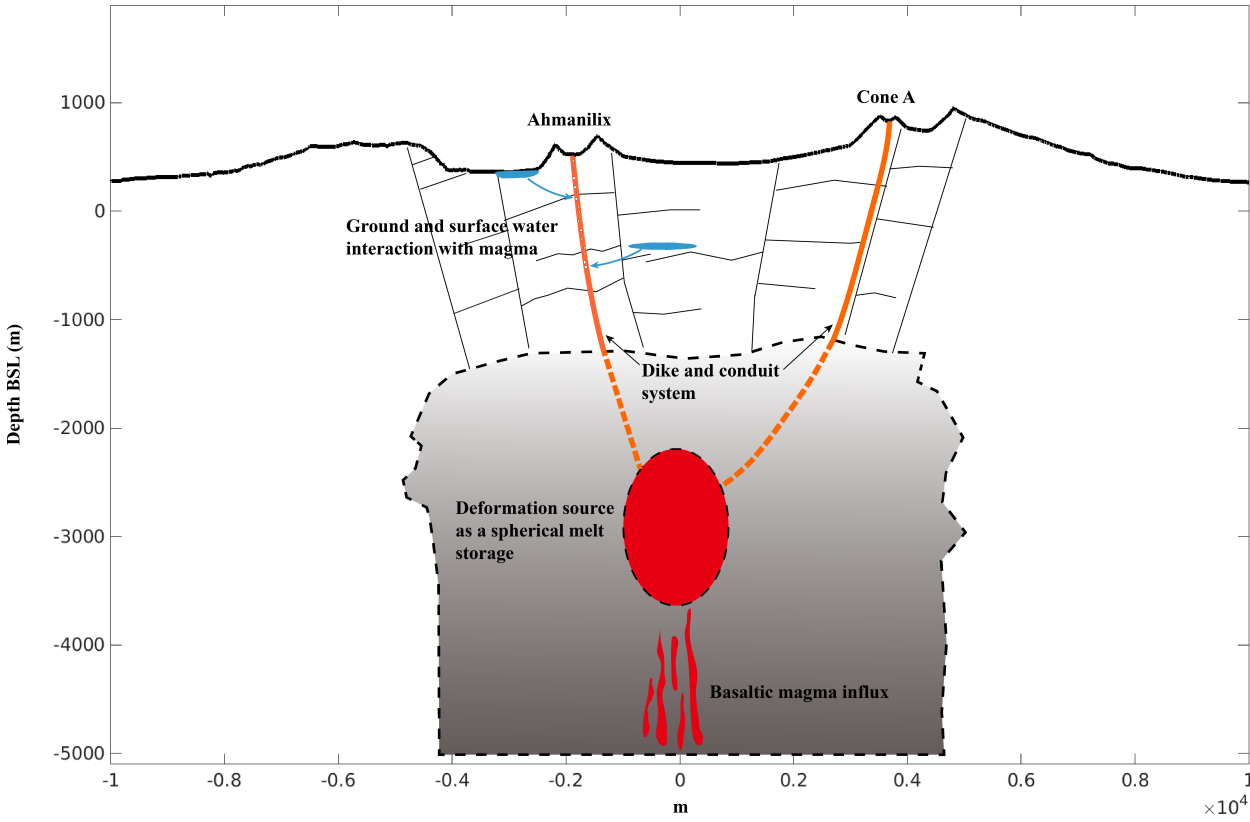


Figure 8. Schematic cross section through Okmok along Cone A and Ahmanilix illustrating the mechanism for the proposed over extrusion. The 2008 eruption was fed possibly by dike systems well evolved during the caldera collapse. Interaction between the magma ascent and ground and surface water may also contributed to the large eruption volume.

5. Conclusion

In this paper, we have mapped the inflation of Okmok volcano after the 2008 eruption with the PS-SBAS method. Multi-temporal SAR datasets from C-band Envisat and Sentinel-1, X-band TerraSAR-X and L-band ALOS-2 over long-period observations allow us to produce deformation time-series with high accuracy within the caldera, despite the dense APS artifacts contamination. The generated deformation history indicates Okmok has been inflating at a time-varying rate ranging from about $30 - 150 \, mm/yr$ since after the 2008 eruption, which agrees well with the CGPS records. We then track the magma system evolution with EnKF using a spherical incompressible pressure source. The results suggest that the volcanic deformation can be explained well by a source located about $3 \, km$ BSL at the center of the caldera with little variations in lateral positions, which we believe, is the same source that produced the 1997 and 2008 eruptions and the surface deformation associated with them. The cumulative volume change accounting for the inflation is about $0.08 \, km^3$ from 2008 to 2020, which is about 160% and about 60% of the total reservoir volume changes during the 1997 and the 2008 eruptions, respectively.

The dense SAR data acquisitions from spaceborne SAR sensors such as Sentinel-1 provides critical constraints for the mapping of volcanic deformation, and EnKF is a promising tool to

- assimilate the time-series deformation for the determination of source location and the tracking
- of temporal evolution of the source strength. The combination of InSAR and EnKF provides an
- exquisite approach to update the source evolution of volcanoes for hazards forecasting and
- prevention. However, although elegant source modeling can be produced with current workflow
- and datasets, limitations still remain. For example, the poor data coverage in certain areas due to
- decorrelation in long-term observations may compromise the performance of EnKF as that in our
- study during 2008 to 2014, no coherence for winter acquisitions of C-band SAR can make it
- difficult to track the deformation continuously, saturation of dense APS artifacts may degrade the
- data coverage significantly in order to get robust inversions. Hopefully, this situation can be
- solved provided high interferometric-quality SAR data, e.g., the future NISAR mission, and new
- algorithms that are capable of dealing with decorrelation and APS contaminations.

Acknowledgments, Samples, and Data

- This research is funded by NASA Earth Surface & Interior Program (80NSSC19K0357),
- NASA NISAR Science Team (80NSSC19K1491), and the Shuler-Foscue Endowment at the
- Southern Methodist University. ALOS-2 PALSAR-2 datasets are copyrighted and provided by
- Japan Aerospace Exploration Agency's via the 2nd Research Announcement on the Earth
- Observations (PI No. ER2A2N061). Constructive comments from the Associate Editor Emma
- Hill, Prof. Sigurjon Jonsson and Prof. Manoochehr Shirzaei improved the manuscript.

630 Data Availability Statement

- InSAR deformation time series and modeling results are available at "Figshare"
- 632 (10.6084/m9.figshare.14602983)

References

623

633

637

642

646

650

- Albright, J. A., Gregg, P. M., Lu, Z., & Freymueller, J. T. (2019). Hindcasting magma reservoir
- stability preceding the 2008 eruption of Okmok, Alaska. Geophysical Research Letters, 46,
- 636 8801–8808. https://doi.org/10.1029/2019GL083395
- 638 Biggs, J., Lu, Z., Fournier, T., & Freymueller, J. T. (2010). Magma flux at Okmok volcano,
- Alaska, from a joint inversion of continuous GPS, campaign GPS, and interferometric synthetic
- aperture radar. Journal of Geophysical Research, 115, B12401.
- 641 https://doi.org/10.1029/2010JB007577
- 643 Caricchi L., Biggs J., Annen C., Ebmeier S. (2014), The influence of cooling, crystallization and
- re-melting on the interpretation of geodetic signals in volcanic systems. Earth and Planetary
- 645 Science Letters, 288, pp. 166-174, http://dx.doi.org/10.1016/j.epsl.2013.12.002
- 647 Cervelli, P., and A. Miklius (2003), The shallow magmatic system of Kilauea Volcano, in The
- Pu'u 'O'o-Kupaianaha Eruption of Kilauea Volcano, Hawai'i: The First 20 Years, edited by C.
- Heliker et al., pp. 149–164, Prof. Pap. 1676, U.S. Geol. Surv, Reston, Virginia.
- Blewitt, G., W.C. Hammond, C. Kreemer. (2018), Harnessing the GPS Data Explosion for
- Interdisciplinary Science, Eos, 99, https://doi.org/10.1029/2018EO104623.
- Byers, F.M. (1959). Geology of Umnak and Bogoslof Islands, Aleutian Islands, Alaska. U.S.
- Geological Survey Bulletin B; U.S. Government Printing Office: Washington, DC, USA, pp.

656 267–369

657

- Evensen, G., 2003. The ensemble Kalman filter: theoretical formulation and practical
- 659 implementation. Ocean Dyn. 53:343–367. http://dx.doi.org/10.1007/s10236-003-0036-9.

660

- Evensen, G., 2003. The ensemble Kalman filter: theoretical formulation and practical
- implementation. Ocean Dyn. 53:343–367. http://dx.doi.org/10.1007/s10236-003-0036-9.

663

- Evensen, G. (2009). Data assimilation: The ensemble Kalman filter (2nd ed.). Dordrecht, New
- York: Springer. https://doi.org/10.1007/978-3-642-03711-5

666

- 667 Ferretti, A., Prati, C., Rocca, F., (2001). Permanent scatterers in SAR interferometry. IEEE
- Trans. Geosci. Remote Sens., vol. 39, no. 1, pp. 8-20. https://doi.org/10.1109/36.898661

669

- 670 Fournier, T., Freymueller, J., & Cervelli, P. (2009). Tracking magma volume recovery at Okmok
- volcano using GPS and an unscented Kalman filter. Journal of Geophysical Research, 114,
- 672 B02405. https://doi.org/10.1029/2008JB005837

673

- 674 Freymueller, J. T., & Kaufman, A. M. (2010). Changes in the magma system during the 2008
- eruption of Okmok volcano, Alaska, based on GPS measurements. Journal of Geophysical
- 676 Research, 115, B12415. https://doi.org/10.1029/2010JB007716

677

- 678 Goel, K., Adam, N., (2013). Distributed scatterer interferometry approach for precision
- 679 monitoring of known surface de-formation phenomena. IEEE Transactions on Geoscience and
- Remote Sensing, vol. 52, no. 9, pp. 5454-5468. https://doi.org/10.1109/TGRS.2013.2289370.

681

- 682 Gong, G., Meyer, F., Lee, C.W., Lu, Z., and Freymueller, J. (2015). Measurement and
- interpretation of subtle deformation signals at Unimak Island from 2003 to 2010 using Weather
- Model-Assisted Time Series InSAR, Journal of Geophysical Research-Solid Earth, 120, 1175–
- 685 1194, https://doi.org/10.1002/2014JB011384.

686

- 687 Gregg, P. M., & Pettijohn, J. C. (2016). A multi-data stream assimilation framework for the
- assessment of volcanic unrest. Journal of Volcanology and Geothermal Research, 309, 63–77.
- 689 https://doi.org/10.1016/j.jvolgeores.2015.11.008

690

- Hooper, A., Segall, P., and Zebker, H. (2007 a), Persistent scatterer interferometric synthetic
- aperture radar for crustal deformation analysis, with application to Volcán Alcedo, Galápagos, J.
- 693 Geophys. Res., 112, B07407, https://doi.org/10.1029/2006JB004763.

694

- Hooper, A. (2008), A multi-temporal InSAR method incorporating both persistent scatterer and
- small baseline approaches, Geophys. Res. Lett., 35, L16302,
- 697 https://doi.org/10.1029/2008GL034654.

- Hooper, A., H. Zebker, P. Segall, and B. Kampes (2004), A new method formeasuring
- deformation on volcanoes and other natural terrains using InSAR persistent scatterers, Geophys.
- 701 Res. Lett.,31, L23611, https://doi.org/10.1029/2004GL021737.

Hooper, A., Zebker, H. A., (2007 b). Phase unwrapping in three dimensions with application to InSAR time series. J. Opt. Soc. Am. A/ Vol. 24. https://doi.org/10.1364/JOSAA.24.002737

705

McConnell, J.R., and others (2020). Extreme climate after massive eruption of Alaska's Okmok volcano in 43 BCE and effects on the late Roman Republic and Ptolemaic Kingdom. PNAS, 117 (27) 15443-15449. https://doi.org/10.1073/pnas.2002722117

709

Kalman, R.E. (1960). A new approach to linear filtering and prediction problems. J. Fluids Eng. 82, 35–45. https://doi.org/10.1115/1.3662552

712

Larsen, J.F., Neal, C.A., Schaefer, J.R., Kaufman, A.M., and Lu, Zhong, (2015). The 2008 phreatomagmatic eruption of Okmok Volcano, Aleutian Islands, Alaska: Chronology, deposits,

and landform changes: Alaska Division of Geological & Geophysical Surveys Report of

716 Investigation 2015-2, 53 p. https://doi.org/10.14509/29405

717

- Larsen, J.F., Neal, C., Schaefer, J., Beget, J. and Nye, C. (2007). Late Pleistocene and Holocene
- 719 Caldera-Forming Eruptions of Okmok Caldera, Aleutian Islands, Alaska. In Volcanism and
- Subduction: The Kamchatka Region (eds J. Eichelberger, E. Gordeev, P. Izbekov, M. Kasahara
- 721 and J. Lees). https://doi.org/10.1029/172GM24

722

- Lu Z., Dzurisin D. (2014). InSAR Imaging of Aleutian Volcanoes. In: InSAR Imaging of
- Aleutian Volcanoes. Springer Praxis Books. Springer, Berlin, Heidelberg.
- 725 https://doi.org/10.1007/978-3-642-00348-66

726

- Lu, Z., Dzurisin, D., Biggs, J., Wicks, C., & McNutt, S. (2010a). Ground surface deformation
- patterns, magma supply, and magma storage at Okmok volcano, Alaska, from InSAR analysis: 1.
- Intercruption deformation, 1997–2008. Journal of Geophysical Research, 115, B00B03.
- 730 <u>https://doi.org/10.1029/2009JB006969</u>

731

- Lu, Z., & Dzurisin, D. (2010b). Ground surface deformation patterns, magma supply, and
- magma storage at Okmok volcano, Alaska, from InSAR analysis: 2. Coeruptive deflation, July-
- August 2008. Journal of Geophysical Research, 115, B00B02.
- 735 https://doi.org/10.1029/2009JB006970

736

- Lu, Z., Fielding, E., Patrick, M., & Trautwein, C. (2003a) Estimating lava volume by precision
- combination of multiple baseline spaceborne and airborne interferometric synthetic aperture
- radar: The 1997 eruption of Okmok volcano, Alaska. IEEE Trans. Geosci. Remote Sens., 41,
- 740 1428–1436. https://doi.org/10.1109/TGRS.2003.811553

741 742

- Lu, Z., Masterlark, T., Dzurisin, D., Rykhus, R., and Wicks, C. (2003b). Magma Supply
- Dynamics at Westdahl Volcano, Alaska, Modeled from Satellite Radar Interferometry: Journal
- of Geophysical Research, 108 (B7), 2354, https://doi.org/10.1029/2002JB002311.

746

Lu, Z., Mann, D., Freymueller, J. T., and Meyer, D. J. (2000), Synthetic aperture radar

- interferometry of Okmok volcano, Alaska: Radar observations, *J. Geophys.*
- 749 Res., 105(B5), 10791–10806, https://doi.org/10.1029/2000JB900034.
- 750
- Lu, Z.; Masterlark, T.; Dzurisin, D. (2005). Interferometric synthetic aperture radar study of
- Okmok volcano, Alaska, 1992–2003: Magma supply dynamics and post-emplacement lava flow
- deformation. J. Geophys. Res. 110, B2, 0148-0227. https://doi.org/10.1029/2004JB003148

- Mann, D.; Freymueller, J.; Lu, Z. (2002). Deformation associated with the 1997 eruption of
- 756 Okmok volcano, Alaska. J. Geophys. Res., 107, B4, 0148-0227.
- 757 https://doi.org/10.1029/2001JB000163

758

- Miller, D., and others (2020). Linking magma storage and ascent to eruption volume and
- composition at an arc caldera. Geophysical Research Letters, 47, e2020GL088122.
- 761 <u>https://doi.org/10.1029/2020GL088122</u>.

762

- Mirray, K.; Bekaert, D.; Lohman, R. (2019). Tropospheric corrections for InSAR: Statistical
- assessments and applications to the Central United States and Mexico. Remote Sensing of
- 765 Environment, 232, 111326. https://doi.org/10.1016/j.rse.2019.111326

766

- Ohlendorf, S. J., Thurber, C. H., Pesicek, J. D., & Prejean, S. G. (2014). Seismicity and seismic
- structure at Okmok Volcano, Alaska. Journal of Volcanology and Geothermal Research, 278-
- 769 279, 103–119. https://doi.org/10.1016/j.jvolgeores.2014.04.002

770

- Patrick, M.R.; Dehn, J.; Papp, K.R.; Lu, Z.; Dean, K.G.; Moxey, L.; Lzbekov, P.; Guritz, R.
- 772 (2003). The 1997 eruption of Okmok Volcano, Alaska: A synthesis of remotely sensed imagery.
- J. Volcanol. Geotherm. Res., 127, 87–105. https://doi.org/10.1016/S0377-0273(03)00180-X

774

- Porter, C., Morin, P, and others (2018). ArcticDEM, https://doi.org/10.7910/DVN/OHHUKH,
- Harvard Dataverse, v1.

777 778

- Qu, F., Lu, Z., Poland, M., Freymueller, J., Zhang, Q., & Jung, H.-S. (2015). Post-Eruptive
- Inflation of Okmok volcano, Alaska, from InSAR, 2008–2014. Remote Sensing, 7(12), 15839.
- 780 https://doi.org/10.3390/rs71215839

781

- Xue, X., Freymueller, J., & Lu, Z. (2020). Modeling the posteruptive deformation at Okmok
- based on the GPS and InSAR time series: Changes in the shallow magma storage system. Journal
- of Geophysical Research: Solid Earth, 125, e2019JB017801.
- 785 https://doi.org/10.1029/2019JB017801

786

- Zhan, Y., and Gregg, P.M. (2017). Data assimilation strategies for volcano geodesy. Journal of
- Volcanology and Geothermal Research 344 (2017) 13–25.
- 789 https://doi.org/10.1016/j.jvolgeores.2017.02.015

790 791